Mon. Not. R. Astron. Soc. **000**, 1–?? (2003) Printed 30 March 2004 (MN LATEX style file v2.2)

The gravitational wave background from neutron star birth throughout the cosmos

E. Howell, D. Coward, R. Burman, D. Blair and J. Gilmore
School of Physics, University of Western Australia, Crawley WA 6009, Australia

30 March 2004

ABSTRACT
We present calculations of the stochastic gravitational wave (GW) background resulting from neutron star birth throughout the Universe. We update previous calculations by employing three GW waveforms from Dimmelmeier, Font & Müller (2002), based on three models incorporating general relativistic effects for the axisymmetric core collapse of rotating massive stars. Source-rate evolution is accounted for by using a simulated star formation rate model based on a 'flat-Λ' cosmology (Hernquist & Springle 2003). We show that the GW background is only weakly dependent on the source-rate evolution model. Prominent features in the single-source GW spectral strain can be related to the calculated background spectra, even though the features are broadened and redshifted because of contributions from high-redshift sources. The background spectral closure density is reduced by 1–2 orders of magnitude compared to previous calculations, a consequence of using relativistic single-source GW waveforms and a more slowly evolving source-rate density. Duty cycle estimates for this background imply a non-continuous signal, assuming it consists predominantly of 'regular' and 'rapid' core-collapse models. We note that the background may be considerably enhanced by the inclusion of dynamic post-collapse instabilities (bar-modes), which are not included in this work, so our estimates for this background may be lower limits.

Key words: gravitational waves – stars: formation – supernovae: general – cosmology: miscellaneous

1 INTRODUCTION

A stochastic background of gravitational waves (GWs) is a detection target for proposed "Advanced" laser interferometer detectors. Discovery of a stochastic background of *primordial* origin (Carr 1980) would yield unique insight into the earliest moments of the Universe. Detection of a stochastic background of *astrophysical* origin, from core-collapse supernovae (SNe) or other sources distributed throughout the cosmos, would provide a new probe of the high-redshift Universe. Understanding how these two very different backgrounds will accumulate in detector outputs is an important and challenging task.

At present, three long-baseline laser interferometric GW detectors have been, or are nearly, constructed. The US LIGO (Laser Interferometer Gravitational-wave Observatory) consists of two 4-km arm detectors situated at Hanford, Washington, and Livingston, Louisiana. The Italian/French VIRGO project is completing a 3-km baseline instrument at Cascina, near Pisa. Smaller detectors are under construction at Hannover (the German/British GEO project with a 600-m baseline, which had its first test runs in 2002) and Perth (Australian International Gravitational Observatory, AIGO, initially with an 80-m baseline). A detector at Tokyo (TAMA, 300-m baseline) has been taking data since 2001.[1]

The two LIGO detectors have recently begun taking data. By 2007 or so, they will be upgraded to second-generation interferometers ("Advanced LIGO"), which will use advanced technologies and materials presently being tested, including high-power lasers and state-of-the-art vibration-isolation systems. AIGO will be operated as a test facility for Advanced LIGO, for which the stochastic background of GWs is a detection target.

Estimates of the spectral and temporal properties of the stochastic GW background have been made by a number of authors – see the paper by Coward, Burman & Blair (2001; hereafter CBB) for a brief discussion. CBB used a sample of Newtonian gravitational numerical models for the axisymmetric rotational core collapse of massive stars (Zw-

[1] For updates on the status of these projects visit:
LIGO—http://www.ligo.caltech.edu/
VIRGO—http://www.virgo.infn.it/
GEO—http://www.geo600.uni-hannover.de/
AIGO—http://www.gravity.uwa.edu.au/
TAMA—http://tamago.mtk.nao.ac.jp/

erger & Müller 1997; hereafter ZM) to investigate the GW background resulting from those core-collapse events that lead to the formation of neutron stars (NSs). To account for source rate evolution, they used the Einstein-de Sitter cosmology and an observation-based star formation rate (SFR) model, namely Model 1, denoted by Ψ_1, of Madau, Pozetti & Dickenson (1998; hereafter MPD), which assumes little dust extinction at high redshift z. CBB calculated the GW background out to $z = 5$ by integrating the product of the differential rate of NS formation with the single-source fluence. They computed values for the spectral flux density, spectral strain, closure density and duty cycle (DC) of the background, and showed that the background spectrum retained a dependence on the single-source emission spectrum and that a DC close to unity was possible for NS birth sources.

In this paper we revise that work to determine the spectral properties of this GW background using refined simulated waveforms from Dimmelmeier, Font & Müller (2002; hereafter DFM) that incorporate general relativity. We use a 'flat-Λ' cosmology — a spatially flat cosmology with a cosmological constant — and a simulation-based SFR model from Hernquist & Springel (2003; hereafter HS), which allows the integration to be extended to $z = 10$ and beyond. Recent data from the Wilkinson Microwave Anisotropy Probe (WMAP), in conjunction with observations of the Fe/Mg abundance ratio in high-redshift quasars, suggests that star formation started at $z > 9.5$ (Yokoyama 2003). Whereas Fe is predominantly produced by Type Ia SNe, whose progenitor stars have Gyr or greater lifetimes, Mg is produced by core-collapse SNe, which have short-lived progenitors; so the Fe/Mg ratio at z is a measure of the time elapsed between the initial star formation epoch and z.

We also re-calculate the GW background properties using the SFR Model 1 of MPD, and find only a weak dependence on the choice of SFR model; this supports the suggestion of Phinney (2001) that the background is only weakly dependent on the evolutionary history of the sources.

The organization of the paper is as follows: In Section 2, using the SFR model and an estimate of the observed local rate density of SNe out to 10 Mpc, we estimate the differential rate of NS formation throughout the Universe; integrating gives the total rate throughout the Universe as calculated in our frame. In Section 3, we use a selection of three distinctive rotational core-collapse GW waveform types simulated by DFM to compute the single-source spectra, at a fiducial source distance of 10 Mpc, under both Newtonian and relativistic gravity. In Section 4, using the differential rate and single-source spectra from Sections 2 and 3, we calculate the background spectral flux density, spectral strain, closure density and duty cycle for backgrounds consisting of each of the selected relativistic waveforms. In section 5, we discuss the effect of the SFR model on our GW background calculations. In Section 6, we consider the detectability of the background by Advanced LIGO. In Section 7, we discuss our results and indicate how this work may be extended.

2 NS FORMATION RATE

2.1 The local NS birth rate

Discoveries of SNe in nearby galaxies (out to some tens of Mpc) suggest that SN events occur at an average rate of a few per century, or one per 10^9 s, in galaxies like our own, though the rate varies with galaxy luminosity and Hubble type (Cappellaro et al. 1997; Cappellaro, Evans & Turatto 1999). As part of an extensive study of SN event rates in the context of GW detection, Rapagnani (1990) calculated an expected event rate for SNe of all types of about 1 per year within 10 Mpc (or $z \approx 0.002$) of our location. In approximate correspondence with this, we take the local rate density of SNe, $r_0^{\rm SN}$, to be 1×10^{-11} SNe s^{-1} Mpc^{-3}. Assuming that about 65 per cent of SNe in typical spiral galaxies are the result of core collapse (Cappellaro et al. 1999), we take $r_0^{\rm cc} \approx 6.5 \times 10^{-12}$ SNe s^{-1} Mpc^{-3} for the local rate density of core-collapse SNe.

We assume that each core collapse results in either a black hole or a NS. To estimate the branching ratio, we use a stellar initial mass function with a Salpeter exponent, and take a NS progenitor mass range of 8–25 M$_\odot$ and a black hole progenitor mass range of 25–125 M$_\odot$. The resulting rate of NS formation is about four times that of black hole formation. Combined with $r_0^{\rm cc}$ this yields, for the local NS formation rate density, $r_0^{\rm NS} \approx 5 \times 10^{-12}$ NS s^{-1} Mpc^{-3} (see CBB, sect. 2.1, for more details).

As the lifetimes of stars more massive than 8–10 M$_\odot$ are only tens of Myr, the evolving rate of core-collapse SNe closely tracks the SFR (Yungelson & Livio 2000).

2.2 The evolving SFR

Several observation-based models of the evolving SFR have been proposed in recent years (e.g. MPD, Lanzetta et al. 2002). A consensus on the form of SFR evolution has not yet been reached, partly because of systematic uncertainties, such as the amount of dust extinction, and because of the difficulties of the observations. This has motivated us to employ a recent simulation-based model that predicts SFR evolution out to high z, but is still compatible, within present uncertainties, with observation-based models of SFR evolution.

Springel & Hernquist (2003) conducted hydrodynamic simulations using a flat-Λ 'cold dark matter' cosmology to study cosmic star formation from $z \approx 20$ to the present. In addition to gravitation and ordinary hydrodynamics, their model included the effects of star formation feedback processes (via supernovae and stellar winds) on the interstellar medium. We use a fit to this simulation, developed by HS, which includes a scaling related to the expansion rate of the universe, represented by the evolution of the Hubble parameter

$$h(z) \equiv H(z)/H_0 = \left[\Omega_{\rm m}(1+z)^3 + \Omega_\Lambda\right]^{1/2} \qquad (1)$$

for a flat-Λ cosmology ($\Omega_{\rm m} + \Omega_\Lambda = 1$). We take $\Omega_{\rm m} = 0.3$ and $\Omega_\Lambda = 0.7$ for the $z = 0$ density parameters, and $H_0 = 70$ km s^{-1} Mpc^{-1}. The fit takes the form

$$\dot\rho_*\Big[h(z)\Big] = \dot\rho_{*[z=0]} \frac{h^{4/3}}{1 + \alpha(h^{2/3} - 1)^3 \exp(\beta h^{7/6})} \ , \qquad (2)$$

with $\dot\rho_{*[z=0]} = 0.013$ M$_\odot$ yr^{-1} Mpc^{-3}, $\alpha = 0.012$ and $\beta = 0.041$.

HS (sect. 3) gave physical arguments for the general form of this function as an approximate fitting function. The SFR density rises exponentially from high z, reflecting

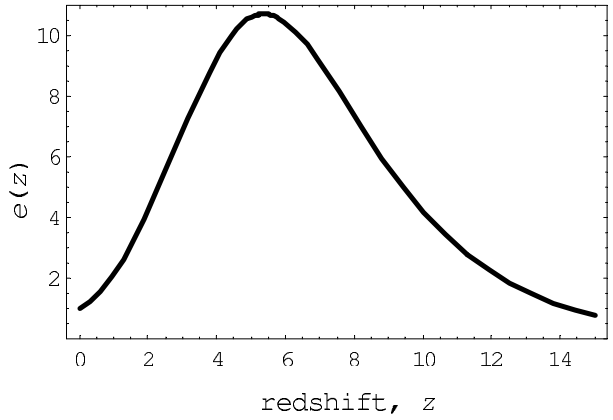

Figure 1. The dimensionless neutron star formation rate density evolution factor $e(z)$, normalized to 1 in our local galactic neighbourhood, based on the SFR simulation model of Hernquist & Springel (2003). It reaches a peak in the redshift range $z = 5 - 6$.

the gravity-driven growth of dark-matter haloes. It reaches a peak at $z \approx 5 - 6$ and declines to $z = 0$ as $h^{4/3}(z)$, in proportion to the cooling rate of the haloes. We have used this SFR evolution model in the form of a dimensionless evolution factor $e(z)$, normalized to the local ($z = 0$) rate, plotted in Figure 1; this expresses the evolution of the NS birth rate density.

We note that this model is quite different from the MPD Model 1 used by CBB, which has a steep rise, by a factor of about 10, for a redshift less than 1.5. The model used here shows an increase out to $z = 1.5$ by a factor of about 3 and a maximum factor of about 12 at $z = 5 - 6$, so the source evolution is biased toward higher z than in Model 1.

2.3 The integrated neutron star formation rate

The variation of the NS formation rate with redshift is described by the event-rate equation

$$\mathrm{d}R^{\mathrm{NS}}/\mathrm{d}z = 4\pi(c^3 {r_0}^{\mathrm{NS}}/{H_0}^3)e(z)F(z)/(1+z)\ , \qquad (3)$$

where $R^{\mathrm{NS}}(z)$ is the all-sky event rate, as observed in our local frame, for sources out to redshift z. The factor $(c^3 {r_0}^{\mathrm{NS}}/{H_0}^3)$ has the dimensions of inverse time, as does the event rate R^{NS}. The $(1+z)$ denominator in (3) accounts for the time dilation of the observed rate by cosmic expansion, converting a source-count equation to an event-rate equation. The dimensionless function $F(z)$ is determined by the cosmological model. For the flat-Λ cosmology used in this study (Peebles 1993, p. 332):

$$F(z) = [\, H_0 d_{\mathrm{A}}(z)/c\,]^{\,2}/h(z)\ , \qquad (4)$$

where $d_{\mathrm{A}}(z)$, the angular size distance, is defined by

$$H_0 d_{\mathrm{A}}(z)/c = \int_0^z \mathrm{d}z'/h(z')\ . \qquad (5)$$

Figure 2 plots $\mathrm{d}R^{\mathrm{NS}}/\mathrm{d}z$ as a function of redshift. It shows that the differential rate reaches a maximum at $z = 3{-}4$, in contrast to a maximum at $z = 1{-}2$ using the Madau et al. (1998) SFR model — see fig. 2 of CBB. Integration of (3) over all z will yield the total rate of NS

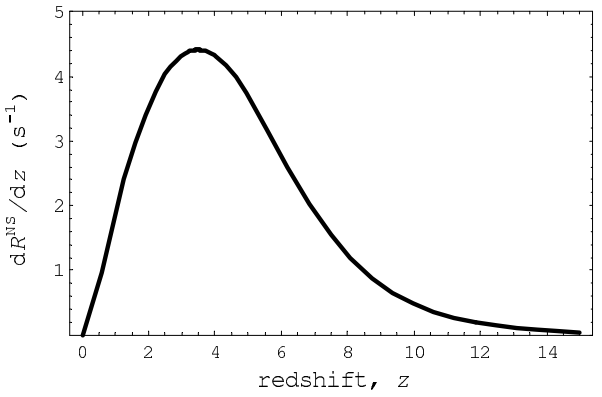

Figure 2. The differential rate of neutron star formation, $\mathrm{d}R^{\mathrm{NS}}/\mathrm{d}z$, as a function of redshift, as observed in our local frame, using a 'flat-Λ' cosmology with $\Omega_{\mathrm{m}} = 0.3$, $\Omega_\Lambda = 0.7$ and $H_0 = 70$ km s^{-1} Mpc^{-1}.

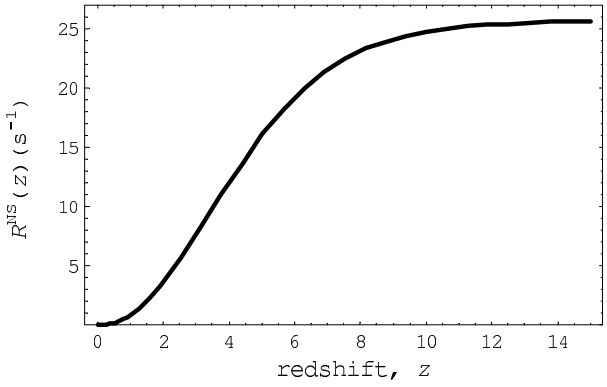

Figure 3. The cumulative NS formation rate as a function of z, as observed in our local frame. It is asymptotic to about 25 s^{-1} — the integrated rate throughout the Universe.

formation throughout the Universe, as potentially observed by us. We integrate (3) to beyond $z = 10$, since star formation is considered to have begun at that epoch (Yokoyama 2003). Figure 3 for $R^{\mathrm{NS}}(z)$ shows that the total rate of NS formation reaches an asymptotic value of about 25 s^{-1}, not significantly different from the value of 17 s^{-1} obtained by CBB from the MPD SFR Model 1 in the Einstein-de-Sitter cosmology with $H_0 = 50\,\mathrm{km\,s^{-1}Mpc^{-1}}$. This is despite our using a SFR model that is biased to higher-z sources and extending the cutoff for NS formation from $z = 5$ to beyond $z = 10$. The steep rise of $R^{\mathrm{NS}}(z)$ at intermediate z is because of the increasing sky surface area and the increasing evolution factor from the SFR model.

3 SPECTRAL PROPERTIES OF A SINGLE SOURCE

3.1 Simulated waveforms

DFM conducted a study of the dynamics of axisymmetric, rotational supernova core collapse using both general relativistic and Newtonian hydrodynamic simulations, thus extending the work of ZM who worked with Newtonian gravity.

Table 1. Quantities associated with the three selected relativistic waveforms from DFM: $f_{\max}$ is the frequency of maximum spectral energy density (table 1 of DFM) and $E_{\rm GW}$ is the total energy radiated in the form of gravitational waves (determined by using the waveforms in eq (3) of DFM). The maximum dimensionless amplitude at a source distance of 10 Mpc is also given (from table 1 and eq (6) of DFM).

Model	Type	$f_{\max}$ [Hz]	Max. amplitude at 10 Mpc [10^{-24}]	$E_{\rm GW}$ [10^{-8} $M_\odot c^2$]
A1B3G3	I	702	5.83	1.19
A3B4G2	II	101	5.26	0.16
A1B3G5	III	904	1.10	0.032

To encompass the many uncertainties, DFM developed 26 core-collapse simulations, each corresponding to a selected combination of three parameters, which determine the initial (pre-collapse) models and serve to catalogue the simulations. These parameters are: a length scale that specifies the degree of differential rotation; the ratio of rotational kinetic energy to the magnitude of the gravitational binding energy; and an adiabatic index, which incorporates (in an extremely simplified way) all the complex microphysics, such as electron capture and neutrino transport.

The GW signals obtained by DFM were found to be within the sensitivity range of first-generation laser interferometer detectors for sources located within the Local Group.

Zwerger (1995), using Newtonian simulations, first identified 3 different classes of axisymmetric core-collapse events, Type I, Type II and Type III, classified by 3 phases of supernova collapse: infall, bounce and ring-down. The infall phase is the result of the initial gravitational instability caused by a sudden softening of the equation of state (EoS). During the bounce phase, the EoS is stiffened due to repulsive nuclear forces becoming opposed by the large inertia and infall kinetic energy, producing a shock wave at the outer edge of the inner core. As the inner core approaches equilibrium the ring-down phase begins.

The Type I waveforms, from a 'regular collapse model', are characterized by a distinct spike, the result of core bounce, followed by a damped oscillation or 'ringdown'. Type II waveforms are typified by several distinct spikes resulting from multiple core bounces. A very rapid core collapse will result in a Type III waveform, which shows no apparent spike but is characterized by a maximum amplitude occurring at the first positive peak, followed by smaller negative and positive amplitudes pre- and post-bounce.

The three categories of collapse identified in the Newtonian simulations were also found to be present in the relativistic simulations, although some models were found to change type, because of higher central densities, on going over to relativistic gravity. For all models that remained of the same type in Newtonian and relativistic simulations, the GW signal displayed smaller amplitudes under relativistic gravity, as a more centrally condensed core can give rise to a smaller GW signal than a denser, but less centrally condensed one. The larger average and peak central densities of the relativistic models also produced increases in the oscillation frequencies of the inner core during the ring-down phase in a regular collapse, and decreases in the time intervals between consecutive bounces in multiple-bounce models. Table 1 lists some key parameters for the selected relativistic waveforms used in this study.

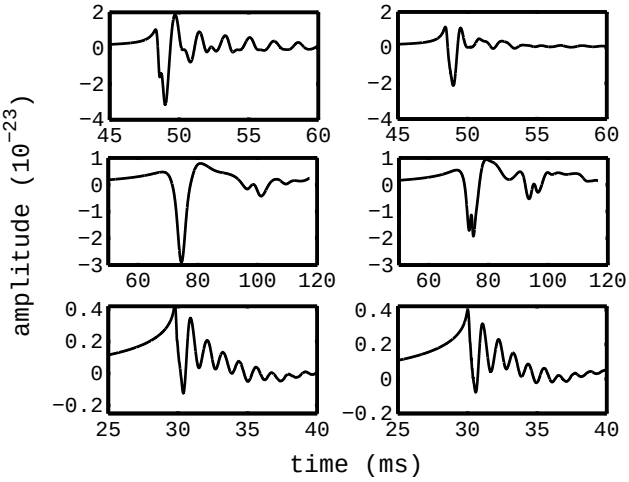

Figure 4. Selected simulated Newtonian (left) and relativistic (right) GW waveforms at a source distance of 10 Mpc, from the DFM catalogues. **Top** – The Type I, 'regular collapse model', waveforms catalogued as 'A1B3G3': a lower amplitude is displayed by the relativistic waveform for the whole duration of the signal. **Middle** – The Type II waveforms catalogued as 'A3B4G2': these, resulting from multiple core bounces, are characterized by several distinct spikes and are of lower amplitude in the relativistic simulation. **Bottom** – The Type III waveforms catalogued as 'A1B3G5': the products of a very rapid core collapse, these show the least change in amplitude and shape between the Newtonian and relativistic simulations.

3.2 Single-source spectra

The spectral time-integrated flux density or spectral fluence, in J m^{-2} Hz^{-1}, of a quadrupole GW signal at a luminosity distance $d_{\rm L}(z)$ from a single source can be expressed as (Ferrari, Matarrese & Schneider 1999)

$$F_{\rm ss}(f,z) = (c^3/8\pi G) f^2 \left|\tilde{A}(f)\right|^2 / \left[d_{\rm L}(z)\right]^2 . \qquad (6)$$

Here $\tilde{A}(f)$, which is in m Hz^{-1}, is the Fourier transform of the wave amplitude (in metres) at the observed frequency f, which is related to the source frequency $f_{\rm source}$ by the redshift factor: $f = f_{\rm source}/(1+z)$. The factor $(c^3/8\pi G)$ has dimensions mass/time, equivalent to energy/(area × frequency).

A spectral strain $\sqrt{S_{\rm h}}$, in Hz$^{-1/2}$, for a single source at redshift z can be expressed in terms of the Fourier transform of the wave amplitude by

$$\sqrt{S_{\rm h}(f,z)} = f^{1/2} \left|\tilde{A}(f)\right| / d_{\rm L}(z) . \qquad (7)$$

The calculated spectral fluence and spectral strain for a source at a fiducial distance of 10 Mpc are shown in Figs 5 and 6.

3.3 Numerical results for single-source spectra

The single-source spectral fluence for the selected Newtonian and relativistic waveforms used in this study are shown in Figure 5. For all three relativistic waveforms, the maxima

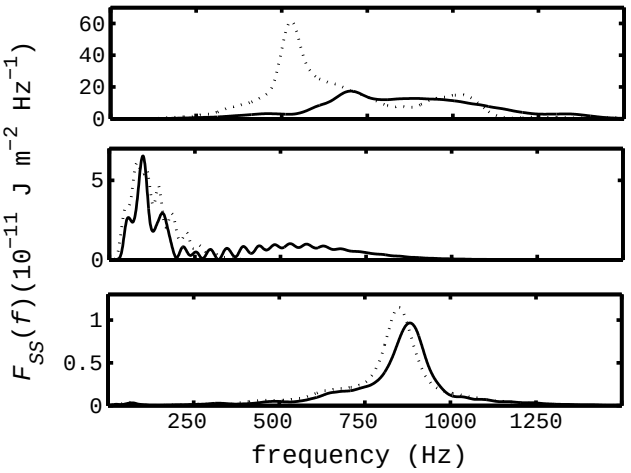

Figure 5. The spectral fluence, at a source distance of 10 Mpc, for selected relativistic (solid lines) and Newtonian (dotted lines) waveforms computed by DFM. A shift of the maximum amplitude towards higher frequencies is apparent in each relativistic waveform as compared with the corresponding non-relativistic waveform, although the shift is small in the Type II and III cases. **Top** – The Type I relativistic waveform displays a smaller maximum, 17×10^{-11} J m^{-2} Hz^{-1} at 700 Hz, shifted by 170 Hz from the Newtonian value. **Middle** – The Type II relativistic waveform peaks at 6.5×10^{-11} J m^{-2} Hz^{-1} at 100 Hz, a shift of 20 Hz from the Newtonian value; it exhibits high-frequency components not visible in the Newtonian waveform. **Bottom** – The maximum for the relativistic model is 1.1×10^{-11} J m^{-2} Hz^{-1} at 850 Hz, 30 Hz higher than for the Newtonian waveform.

occur in about (10^{-11}–10^{-10}) J m^2 Hz^{-1}. The Type I relativistic waveform has a smaller maximum than the corresponding Newtonian waveform, as a result of the smaller amplitude apparent in both the core-bounce and ringdown phases of the relativistic waveform (Fig. 4).

Figure 5 shows that there is a shift towards higher frequencies for the relativistic waveforms in comparison with the Newtonian ones, particularly for the Type I case. Increases in the oscillation frequencies of the inner core during the ring-down phase are responsible for the increase in the dominant emission frequency for waveforms simulated using relativistic gravity in the Types I and III models (DFM). The Type II relativistic waveform also gains a broad high-frequency component, a result of decreases in the time interval between consecutive bounces; DFM calculated an increase of 136% in the arithmetic mean value of peak frequencies for the Type II waveforms due to this effect.

The single-source spectral strain curves, shown in Fig. 6, exhibit maxima of around (10^{-25}–10^{-24}) Hz$^{-1/2}$ for all of the selected waveforms. The Types I and III relativistic waveforms show additional maxima at low frequencies, a feature also apparent in the spectral energy distributions given by DFM for Type I waveforms.

4 A GW BACKGROUND FROM NS FORMATION

4.1 Background spectra

The background spectral flux density, in W m^{-2} Hz^{-1}, from all NS births throughout the Universe is obtained by integrating the product $F_{\rm ss}(f,z)\mathrm{d}R^{\rm NS}/\mathrm{d}z$ over the redshift range $z = 0$ to 10:

$$F_B(f) = \int_0^{10} [\, F_{\rm ss}(f,z)(\mathrm{d}R^{\rm NS}/\mathrm{d}z)\,]\, \mathrm{d}z\,, \tag{8}$$

with the integrand given by (3) and (6). The background spectral strain, in Hz$^{-1/2}$, is calculated directly from this quantity (Ferrari et al. 1999):

$$\sqrt{S_B(f)} = \left(2G/\pi c^3\right)^{1/2} f^{-1}\, [\, F_B(f)\,]^{1/2}\,. \tag{9}$$

The spectral energy density of a GW background is conventionally expressed by the dimensionless 'closure density', $\Omega_{\rm B}(f)$, defined as the energy density of GWs per logarithmic frequency interval normalized to the cosmological critical energy density $\rho_c c^2$; it also can be obtained from $F_{\rm B}(f)$ (Ferrari et al. 1999):

$$\Omega_B(f) = f\, F_B(f)/(\rho_c c^3)\ . \tag{10}$$

The duty cycle (DC) from sources out to redshift z can be approximated by

$$\mathrm{DC}(z) = \int_0^z\ (1+z')\tau(\mathrm{d}R^{\rm NS}/\mathrm{d}z')\,\mathrm{d}z'\,, \tag{11}$$

where the typical duration τ of a signal is dilated to $(1+z)\tau$ by the cosmic expansion. A calculated DC of unity or greater implies that the signal is continuous. If the calculated DC $\leqslant$ 1, then the amplitude distribution can be simulated (Coward et al. 2002a, 2002b) from a random sampling of the probability distribution based on the event rate equation (3).

The numerical values of τ for the three waveform types were estimated using the T_{90} durations of the time-limited gravitational waveforms, defined as the interval in which the signal contains 90% of its energy. (This technique is used in estimating the durations of gamma-ray bursts, for which the duration is calculated as the time interval in which the burst contains between 5% and 95% of its counts.) We determined τ values of 1 ms for the relativistic Type I signal, 22 ms for the Type II signal and 5 ms for the Type III signal. Our estimated T_{90} value for the relativistic Type I waveform is low because of the highly damped ringdown in this case. The Type II relativistic waveform's T_{90} value of 22 ms is greater than the corresponding value of 7 ms for the Newtonian waveform; this is a result of the energy content of the Newtonian waveform being focused around the main spike, while the relativistic Type II waveform's additional high frequency components stretch out the overall energy content for a longer transient duration.

4.2 Numerical results for background spectra

Here only the relativistic waveforms are employed. Figure 7 plots the GW background spectral flux density, obtained from (8), assuming the background to consist of one of the above waveforms. Comparison between the spectral fluence for a single source at 10 Mpc (solid lines in Fig. 5) and the

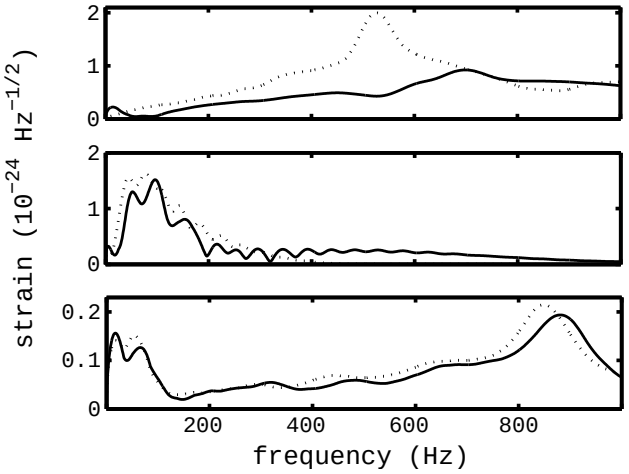

Figure 6. The spectral strain, at a source distance of 10 Mpc, for selected relativistic (solid lines) and Newtonian (dotted lines) waveforms computed by DFM. As was apparent for the spectral fluence, the maximum amplitudes are shifted to higher frequencies under relativistic gravity. **Top** – The Type I relativistic waveform displays a smaller maximum spectral strain, 1×10^{-24} Hz$^{-1/2}$ at 700 Hz, than the Newtonian waveform, which peaks at 2×10^{-24} Hz$^{-1/2}$ at 530 Hz. **Middle** – The Type II waveforms both peak at around 1.5×10^{-24} Hz$^{-1/2}$ in the band (70 – 100) Hz, but the relativistic one exhibits high-frequency components not visible in the Newtonian waveform. **Bottom** – The maxima for the relativistic and Newtonian models are 1.9×10^{-25} Hz$^{-1/2}$ at 880 Hz and 2.2×10^{-25} Hz$^{-1/2}$ at 850 Hz respectively; the two waveforms display a similar spectral spread.

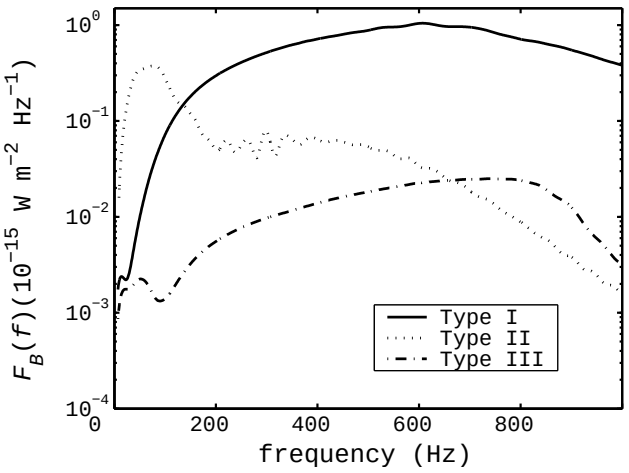

Figure 7. The background spectral flux density using the three selected relativistic waveforms. The maxima for the Types I and II waveforms occur at 1×10^{-15} W m^{-2} Hz^{-1} and 4×10^{-16} W m^{-2} Hz^{-1} at frequencies of 600 Hz and 80 Hz respectively. The Type III peak is over an order of magnitude lower.

background spectral flux density shows that the background spectral features are broadened and shifted to lower frequencies. This is particularly evident for the Type II waveform: the spectral features clearly visible in the single-source fluence are smeared out, a result of the high-z source contributions. The maximum values of the background spectral flux density for the Type I and II waveforms occur at around

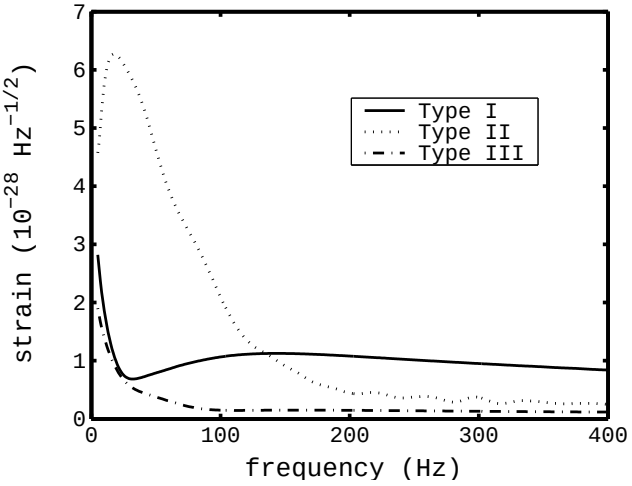

Figure 8. The background spectral strain using the three selected relativistic waveforms. The spectral features visible in the single-source strain spectra (solid lines in Fig. 6) are shifted to lower frequencies and broadened. The Type II curve displays a clear maximum of 6×10^{-28} Hz$^{-1/2}$ at 18 Hz. The Types I and III curves display very broad maxima at around 150 Hz.

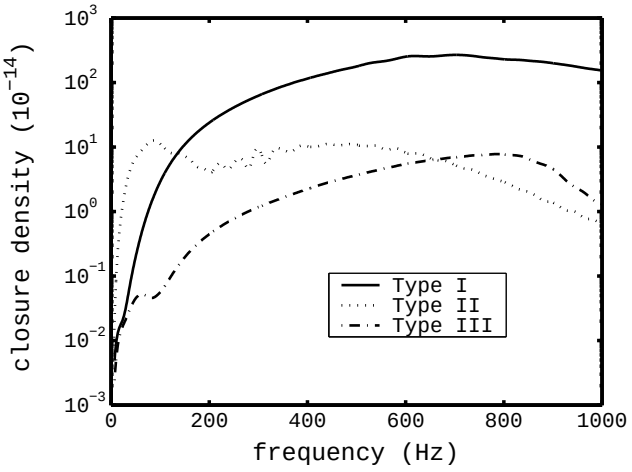

Figure 9. Closure density for a stochastic GW background using the relativistic waveforms. The closure density for the Type I waveform reaches a maximum of 3×10^{-12} at 700 Hz. The Type II and III waveforms peak at about 10^{-13} near 100 Hz and 800 Hz respectively.

(10^{-16}–10^{-15}) W m^{-2} Hz^{-1}, over an order of magnitude above that for the Type III waveform.

Figure 8 shows the background spectral strain for the three selected relativistic waveforms. Prominent features in the single-source spectral strain (solid lines in Fig. 6) for all three waveforms have been broadened and shifted to lower frequencies by a factor of about 5 — a result of the maximum in $\mathrm{d}R^{\mathrm{NS}}/\mathrm{d}z$ occurring at $z \approx 4$. Low-frequency secondary maxima for the Type I and III waveforms, evident in the single-source strain (Fig. 6) at around 20 Hz, manifest as low-frequency ramps in the background strain, a result of the inverse frequency factor in (9) for $\sqrt{S_B(f)}$.

The Type I and Type III waveforms yield very broad maxima at around 150 Hz whereas the Type II waveform

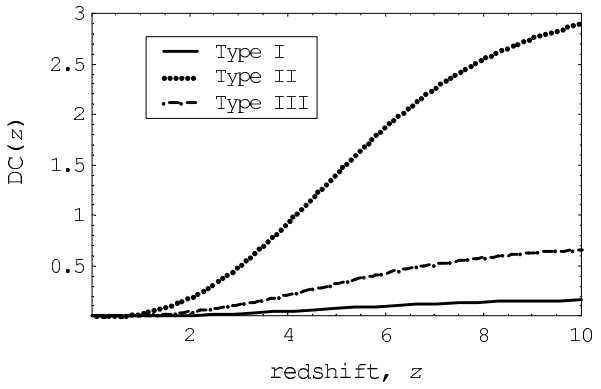

Figure 10. Duty cycle as a function of redshift for backgrounds consisting of one of the 3 relativistic waveforms. Typical values of τ for the three types were estimated using the T^{90} durations of the time-limited gravitational waveforms. The duty cycles of the Type I and Type III waveforms imply a signal described as 'popcorn noise'.

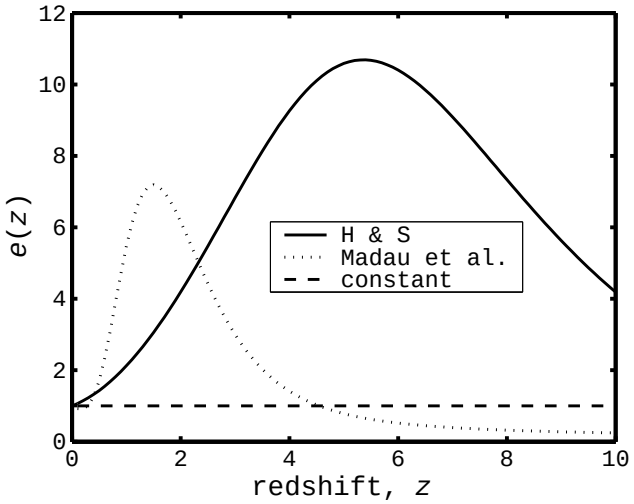

Figure 11. The dimensionless SFR density evolution factors $e(z)$, based on the SFR models Ψ_1 of Madau et al. (1998) and of Hernquist & Springel (2003). The evolution factors are normalized to 1 in our intergalactic neighbourhood. We use a 'flat-Λ' cosmology with $\Omega_{\rm m} = 0.3$, $\Omega_\Lambda = 0.7$ and $H_0 = 70$ km s^{-1} Mpc^{-1}. The constant (non-evolving) SFR density model will be used for comparison.

gives a distinct maximum of about 6×10^{-28} Hz$^{-1/2}$ at 18 Hz; in contrast, CBB found their selected Newtonian Type I waveform to yield a clear maximum. This difference is attributable to several factors: The Type II waveform chosen in this study has most of its flux at lower frequencies than the one used by CBB (see their fig. 5), whilst the Type I relativistic waveform has been shifted to higher frequencies in comparison with the Newtonian one (see Fig. 5); the inverse frequency factor in (9) enhances the Type II background strain reported here. Also, the background spectral flux density for the Type I waveform in CBB was more dominant — 2 orders of magnitude and more greater than for the Type II (see CBB, fig. 7).

The closure density for the relativistic waveforms is shown in Fig. 9. The Type I background has a maximum of about 3×10^{-12} at 700 Hz. The Types II and III peaks at about 10^{-13}, over an order of magnitude lower, are near 100 Hz and 800 Hz respectively. Overall we find that values for the closure density are $1-2$ orders of magnitude smaller than the results presented in fig. 9 of CBB.

The duty cycle estimates for the three relativistic waveforms are displayed in Fig. 10. The results for the Types I and III waveforms imply a non-continuous signal, of a type known as 'popcorn noise'. The high value of τ for the Type II waveform (as discussed in Section 4.1) results in DC(z) > 1 for $z > 4$. The selected Type II waveform was one of the 26 core-collapse models computed by DFM, from which only 2 where found to be of Type II under both Newtonian and relativistic gravity. Our choice of Type II waveform was made so as to draw a representative comparison between the three waveform types and to retain consistency with the work of CBB. Its high DC is of questionable significance, as its amplitude is quite small for much of its (comparatively long) duration — see Fig. 4. Figure 10 shows that for $z < 4$ — the region of most substantial fluence contribution — this waveform yields a DC in the non-continuous regime.

The methods employed here to determine a background from given single-source spectra are appropriate for low-DC backgrounds, consisting of largely non-overlapping wave trains. For backgrounds of DC approaching unity, interference effects must be incorporated. This could be done using the procedure developed by Quilis, Ibáñez, & Sáez (2000) in the context of combining the secular (Gyr timescale) gravitational perturbations caused by the formation of galaxy clusters, each cluster being treated as a single source. Their technique involves imagining a rudimentary detector consisting of two test particles A and B, at some fiducial distance from one of the sources. The strain produced by the source in the detector is proportional to $\sin^2\theta$, where θ is the angle between the line segment AB and the line of sight to the source. If $\theta = \pi/2$, AB is orthogonal to the line of sight and the deformation produced is a maximum, independent of the orientation of AB in the plane perpendicular to the line of sight; if $\theta = 0$, the detector is in the line of sight and no deformation is produced, as the waves are transverse. A mean strain is obtained by averaging over orientations of AB.

5 THE EFFECT OF THE SFR MODEL ON THE BACKGROUND

Because of the uncertainties in SFR modelling, it is important to compare the effect on the GW background of using different proposed SFR models. For comparison, we have recalculated the background properties using the SFR model Ψ_1 (Model 1 of MPD).

An observation-based SFR density is cosmology-dependent, because its deduction is from an observed spectral luminosity in a set volume – so the comoving volume element (based on coordinates attached to the expanding cosmic substratum) and the square of the luminosity distance are involved, the relevant factor being ${d_L}^2/dV_c$ (Woods & Loeb 1998, appendix). The outcome (Porciano & Madau 2001, appendix) is that $\rho_\star$ is proportional to $H(z)$; this is given by equation (1) for flat-Λ cosmologies, including the

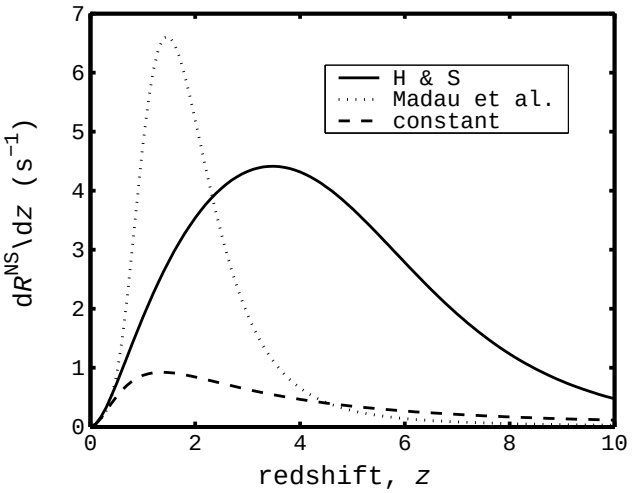

Figure 12. The differential rate of neutron star formation, $\mathrm{d}R^{\mathrm{NS}}/\mathrm{d}z$, as a function of redshift, as potentially observed in our local frame, using the three SFR density evolution factors of Fig. 11.

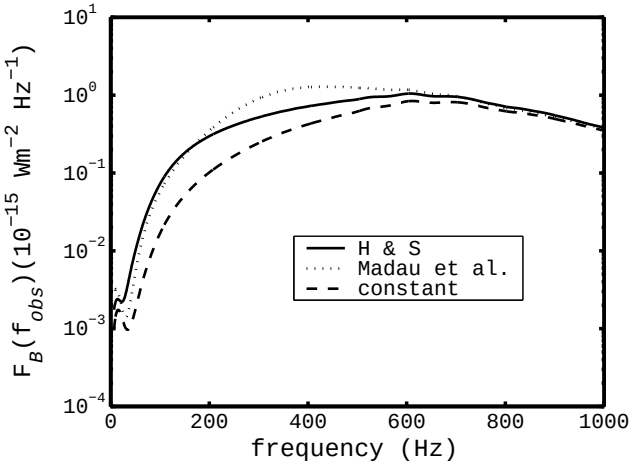

Figure 13. The background spectral flux densities for the Type I relativistic waveform, calculated using the SFR evolution factors of Fig. 11. The three backgrounds display very similar spectra.

limiting case of the Einstein-de Sitter cosmology ($\Omega_m = 1$, $\Omega_\Lambda = 0$).

Because observational determination of even the $z = 0$ SFR density involves distances beyond direct measurement, that quantity is H_0-dependent. Therefore, normalization of the SFR density by its present value to produce an evolution factor $e(z)$ causes the H_0 factors to cancel. As a result, $e(z)$ varies with cosmology as the dimensionless Hubble parameter $h(z) \equiv H(z)/H_0$.

For comparison with the HS SFR model, we have scaled Ψ_1 (which was originally presented for the Eintein-de Sitter cosmology) to the specified 'flat-Λ' cosmology. This reduces the peak value of $e(z)$ by a factor of about 5 from that used by CBB (see their fig. 1). The evolution factors of the HS and re-scaled MPD SFR models are shown in Fig. 11, along with a non-evolving SFR density for comparison.

Figure 12 plots $\mathrm{d}R^{\mathrm{NS}}/\mathrm{d}z$ as a function of redshift using these evolution factors. The differential rate calculated using

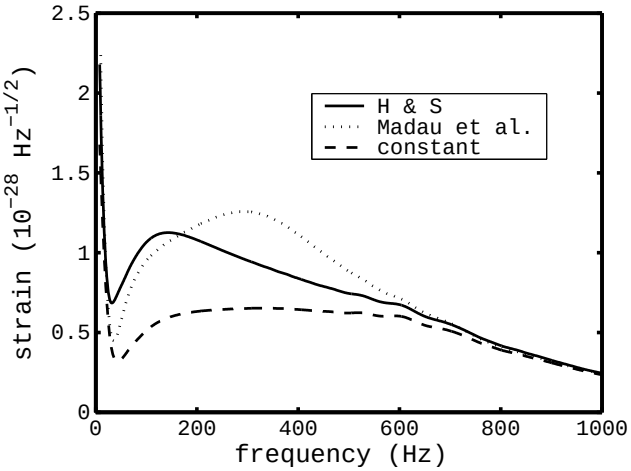

Figure 14. The background spectral strains for the Type I relativistic waveform, calculated using the SFR evolution factors of Fig. 11. The strain calculated from the Madau et al. (1998) model peaks at a higher frequency than that calculated from the HS model.

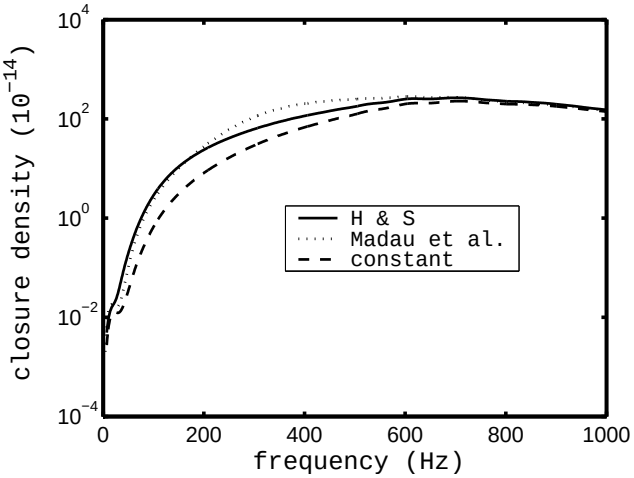

Figure 15. Closure density for a stochastic GW background of Type I relativistic waveforms, calculated using the SFR evolution factors of Fig. 11. Similarities between the three backgrounds, seen in the background spectral flux density (Fig.13), are again apparent.

the constant evolution factor has a maximum of 1 near $z = 1$. The MPD Model 1 gives a maximum of 6.5 near $z = 1.5$, and the HS model gives a maximum of 4.5 near $z = 4$.

Figure 13 compares the GW background spectral flux density calculated from (8) using the three differential rates. The background fluxes are very similar above 600 Hz, indicating a preponderance of low-redshift contributions — a result of the growth of $\mathrm{d}R^{\mathrm{NS}}/\mathrm{d}z$ in the range $0 < z \lesssim 0.5$. The frequency range $(100 - 500)$ Hz shows the greatest deviation between the models, corresponding to the intermediate-z sources, in $0.5 \lesssim z \lesssim 3.5$. The flux using the Ψ_1 model is greatest in that range of intermediate-z sources as a result of the peaking there of the differential rate. The maximum of the HS-based differential rate occurs at about $z = 4$, but the effect of these high-z sources is diminished because of the in-

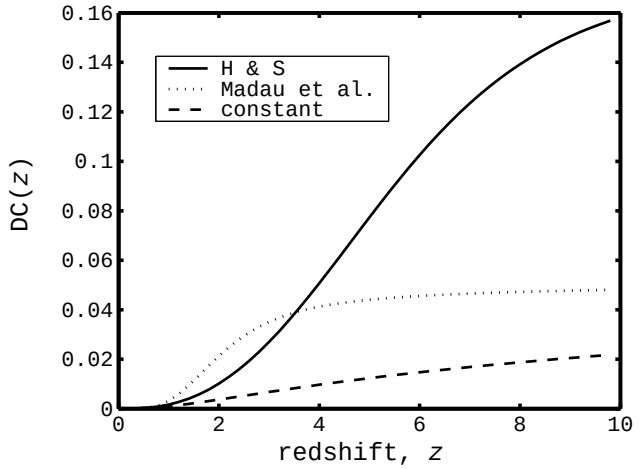

Figure 16. Duty cycle as a function of redshift for backgrounds consisting of Type I relativistic waveforms, calculated using the SFR evolution factors of Fig. 11. All three duty cycles imply non-continuous signals.

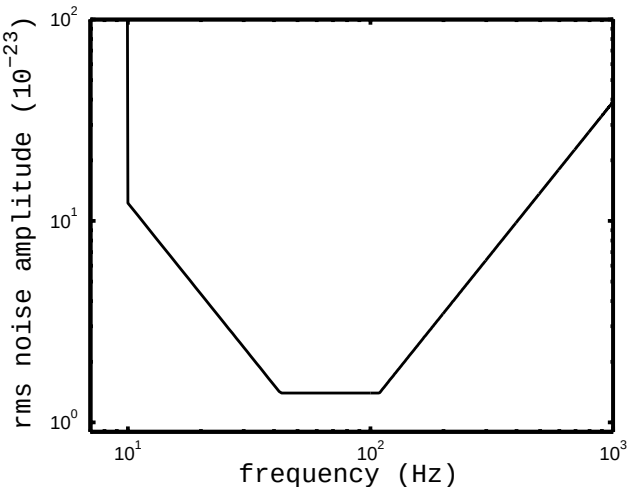

Figure 17. The root-mean-square noise amplitude for an Advanced LIGO detector according to the piecewise parametrized model of Flanagan & Hughes (1998).

verse luminosity distance squared factor in the background flux.

The corresponding background spectral strains, obtained from the spectral flux density via (9), are shown in Fig. 14. The strain based on Ψ_1 has its broad maximum at a higher frequency than for the HS-based calculation — a result of the MDP differential rate peaking at lower z. As found in the previous section (Fig. 8), the low-frequency maximum in the Type I single-source spectral strain (Fig. 6) combines with the $1/f$ factor in (9) for $\sqrt{S_B(f)}$ to produce the low-frequency ramps in Fig. 14.

Figure 15 shows the closure densities calculated from (10) using the three background spectral flux densities. In correspondence with the background flux — as is to be expected from equation (10) and Fig. 13 — the closure density using Ψ_1 is slightly bigger than the HS-based one in the range (200 – 600) Hz.

Figure 16 shows that the DC for the Type I waveform calculated from (11) using Ψ_1 is a little bigger than that estimated using the HS model over the range $1 \lesssim z \lesssim 3.5$, after which it shows no significant growth. All three DCs imply non-continuous 'popcorn noise' signals.

6 DETECTABILITY

The most promising detection strategy is that of cross-correlation of the output of two neighbouring detectors, as reviewed by Allen & Romano (1999) and Maggiore (2000). For the signals in them to be correlated, the detectors must be separated by less than one reduced wavelength, which is about 100 km for frequencies around 500 Hz where $\Omega_{\rm B}(f)$ might peak. The detectors also need to be sufficiently well separated that their noise sources are largely uncorrelated.

Under these conditions, assuming Gaussian noise in each detector and optimal filtering, a filter function chosen to maximize the signal-to-noise ratio, S/N, for two such detectors yields the formula (Allen & Romano 1999, eq. [3.75])

$$\left(\frac{\rm S}{\rm N}\right)^2 \approx \frac{9H_0^4}{50\pi^4} T \int_0^\infty \frac{\gamma^2(f)\Omega_B^2(f)}{f^6 S_{n1}(f) S_{n2}(f)}\,{\rm d}f\,. \qquad (12)$$

Here $\gamma(f)$ is an 'overlap reduction function', which accounts for the separation and relative orientation of the detectors, and $S_{n1}(f)$ and $S_{n2}(f)$ are the noise power spectral densities of the detectors; T is the integration time. As the optimal filter depends on $\Omega_B(f)$, a range of filter functions based on theoretical expectations of this function will need to be used. We have used this definition of S/N so that the growth is linear in the cross-correlation statistic.

For this preliminary study of the detectability of the NS-birth-generated background, we assume an optimized value of close to unity for $\gamma(f)$ of two detectors situated within several km. We take the $\Omega_B(f)$ curves as shown in Fig. 9 and use a piecewise parametrized model for $S_{n1}(f)$ and $S_{n2}(f)$ for proposed Advanced LIGO detectors (Flanagan & Hughes 1998, sect. 4), assuming a pair of similar detectors. This model is expressed in terms of the dimensionless root-mean-square noise amplitude:

$$h_{\rm rms}(f) = \begin{cases} \infty & f < f_s \\ h_m(\alpha f/f_m)^{-3/2} & f_s \leqslant f \leqslant f_m/\alpha \\ h_m & f_m/\alpha \leqslant f \leqslant \alpha f_m \\ h_m[f/(\alpha f_m)]^{3/2} & \alpha f_m \leqslant f\,. \end{cases} \qquad (13)$$

The lower 'shutoff frequency', f_s, is determined by seismic noise. The $f^{-3/2}$ part of the spectrum represents thermal suspension noise and the $f^{3/2}$ part models the laser shot noise. The intermediate flat region, $h = h_m$, provides a transition between these two spectral components; its width is determined by the dimensionless parameter α. The fitting parameters for an Advanced LIGO detector are: $f_s = 10$ Hz, $f_m = 68$ Hz, $\alpha = 1.6$ and $h_m = 1.4 \times 10^{-23}$. The resulting noise curve is shown in Figure 17. The noise power spectral densities of the detectors are calculated using the relation

$$S_{n1,2}(f) = h_{\rm rms}^2(f)\,/f\,. \qquad (14)$$

Figure 18 shows the representative S/N growth for backgrounds consisting of one of the 3 selected relativistic waveforms, yielding S/N values of order 10^{-6}–10^{-3} for an integration time of $T = 1$ yr. The shift to higher frequencies for the general relativistic simulated waveforms compared to the Newtonian ones has contributed to the small S/N. This

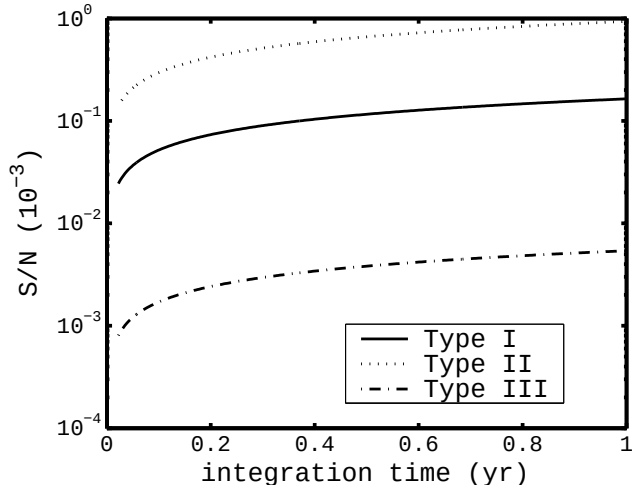

Figure 18. S/N as a function of integration time for backgrounds consisting of one of the 3 selected relativistic waveforms. We assume an optimized configuration of two Advanced LIGO detectors. The S/N value for the Type II waveform is enhanced by its low-frequency components.

is because S/N depends strongly on frequency through the $1/f^6$ factor in the integrand in (12). Also, as a result of this dependence, the Type II waveform's S/N value is enhanced by its low-frequency components.

7 DISCUSSION

7.1 The present results

In this paper we calculate the spectral properties of a GW background resulting from neutron star births throughout the Universe, revising previous calculations (CBB) by employing three general relativistic simulated GW waveforms, based on three models from DFM for the axisymmetric core-collapse of rotating massive stars. Source-rate evolution is accounted for by using a recent simulated SFR model (HS) that is significantly different from the model used earlier. We show that the GW background is only weakly dependent on the source-rate evolution model.

The spectral features of the background spectral strain are broadened and shifted to lower frequencies, because of the contributions from high-redshift sources. Regardless of this, strong spectral features in the single-source spectra can be related to the background spectra. For example, the Type II core-collapse model shows a clear maximum at 18 Hz in the background spectral strain (Fig. 8), corresponding to the (70–100) Hz peak in the single-source spectrum (Fig. 6). This demonstrates that *strong* single-source spectral features can be identified in background spectra. Prominent low-frequency ramps are also evident for the Type I and III waveforms, a result of low-frequency components in the single-source emission spectra enhanced by the inverse frequency factor in the defining formula for the background spectral strain.

The spectral closure density curves are generally lower than those of CBB by $1-2$ orders of magnitude. These differences arise from several factors. Relativistic dynamics cause an overall decrease in magnitude of the relativistic waveforms, compared to the Newtonian waveforms used by CBB, resulting in smaller-magnitude single-source spectra. Also, the HS SFR model predicts that 75% of stars were formed by $z = 1$, implying little recent star formation; this is reflected in the small growth in $\mathrm{d}R^{\mathrm{NS}}/\mathrm{d}z$ at low redshifts. At high z, contributions to the background are strongly reduced by the inverse luminosity distance dependence of the amplitude.

The DC estimates imply a non-continuous signal for backgrounds consisting predominantly of Type I and III relativistic waveforms, and are within the range of those calculated by CBB (their sect. 3.4). The DC estimate for the Type II waveform implies a continuous background because of additional frequency components forcing a high T_{90} duration. Our choice of Type II waveform differs from that selected by CBB, to highlight the comparison between relativistic and Newtonian waveforms of the same type. The Type II model 'A1B3G1' used by CBB, a Type I under relativistic gravity, results in a DC value rising to 0.2 at $z \sim 10$, implying a non-continuous background.

The GW background calculated in this study is unlikely to be detectable by Advanced LIGO detectors assuming reasonable integration times: The S/N, from cross-correlating the output of two co-located Advanced LIGO detectors for one year, results in values several orders of magnitude below unity for the three core-collapse models.

Detection of an astrophysical GW background originating from core-collapse SNe could provide a new probe of the high-z SFR. In addition, such a background contains information on the single-source population. Hence, a search for an astrophysical GW background would potentially provide a new method to constrain both the single-source event rate and the GW energy emission from core-collapse SNe.

7.2 Future developments

There remains considerable uncertainty in our understanding of the core-collapse process that leads to NS formation. For instance, the core probably does not remain axisymmetric during a SN event. Observational evidence suggests that neutron stars formed from SNe receive kick velocities of order 1000 km/s. A systematic study of supernova explosions by Scheck et al. (2003) using hydrodynamic simulations yields evidence that neutrino-driven convection behind the expanding supernova shock can lead to global asymmetries consistent with observed pulsar kick velocities. This supports previous simulations by Burrows & Hayes (1996), which suggested that anisotropic neutrino radiation was a significant contributor to GW emission from core-collapse SNe. These findings indicate that the GW emission models used here may underestimate the emission, at least for a fraction of SNe.

Recent Newtonian simulations of the GW emission from the SN core-collapse process have included the use of a realistic equation of state (Ott et al. 2003) and microphysics, such as electron capture and neutrino transport (Kotake, Yamada & Sato 2003). These aspects were not included in the studies of DFM, no doubt due to the complexity of combining them with a relativistic treatment of gravity.

Other emission mechanisms that have not been considered in this study include non-radial quasi-normal modes of newborn proto-neutron stars. Recent work suggests that the

frequencies of emission are much lower than those of older cold NSs (Ferrari, Miniutti & Pons 2003), and are within the detection bandwidths of terrestrial GW detectors (below 1 kHz), although there is much uncertainty in the emission energy.

Also, our calculations are for simulated core-collapse models that do not include GW emission processes from post-collapse dynamical instabilities, such as the bar-mode instability. Bar modes associated with NS formation are believed to be strong sources of GWs (Shibata, Baumgarte & Shapiro 2000) and could contribute significantly to the total GW emission associated with nascent NSs. In fact, recent calculations of the GW emission from NS bar modes indicate that the fluence could be orders of magnitude greater than that from the collapsing core. The spectral properties of a GW background resulting from a cosmological population including post-collapse instabilities is potentially a more promising source for detection (Howell et al. 2004).

ACKNOWLEDGMENTS

We gratefully thank H. Dimmelmeier, J. A. Font and E. Müller for the use of their waveform data. The authors thank the referee for raising several significant issues in relation to this work, and particularly for suggesting that we repeat our analysis using the MPD SFR model (see Section 5).

REFERENCES

Allen B., Romano J., 1999, Phys Rev D. 59, 102001
Burrows A., Hayes J., 1996, Phys. Rev. Lett., 76, 352
Cappellaro E., Turatto M., Tsvetkov D. Yu., Bartunov O.S., Pollas C., Evans R., Hamuy M., 1997, A&A, 322, 431
Cappellaro E., Evans R., Turatto M., 1999, A&A, 351, 459
Carr B.J., 1980, A&A, 89, 6
Coward D.M., Burman R.R., Blair D.G., 2001, MNRAS, 324, 1015 (CBB)
Coward D.M., Burman R.R., Blair D.G., 2002a, Class Quantum Grav, 19, 1303
Coward D.M., Burman R.R., Blair D.G., 2002b, MNRAS, 329, 411
Dimmelmeier H., Font, J.A., Müller, E., 2002, A&A, 393, 523 (DFM)
Ferrari V., Matarrese S., Schneider R., 1999 MNRAS, 303, 247
Ferrari V., Miniutti G., Pons J.A., 2003 MNRAS, 342, 629
Flanagan É. É., Hughes S. A., 1998, Phys Rev D, 57, 4535
Hernquist L., Springel V., 2003, MNRAS, 341, 1253 (HS)
Howell E., Coward D., Burman R., Blair D., Gilmore J., 2004, Class Quantum Grav, 21, S551
Kotake K., Yamada S., Sato K., 2003, Phys Rev D, 68, 2003
Lanzetta K.M., Yahata N., Pascarelle S., Chen H-W., Fernández-Soto A., 2002, ApJ, 570, 492
Madau P., Pozetti L., Dickenson A., 1998, ApJ, 498, 106 (MPD)
Maggiore M., 2000, Physics Reports, 331, 6
Ott C.D., Burrows A., Livne E., Walder R., 2003, astro-ph/0307472 v1
Peebles P.J.E., 1993, Principles of Physical Cosmology, Princeton Univ. Press, Princeton NJ
Phinney E.S., 2001, astro-ph/0108028
Porciani C., Madau P., 2001, ApJ, 548, 522
Quilis V., Ibáñez J.M., Sáez D., 2000, A&A, 353, 435
Rapagnani P., 1990, A&A, 229, 28
Scheck L., Plewa T., Janka H.-Th., Kifonidis K., Müller E., 2003, astro-ph/0307352 v1
Shibata M., Baumgarte W., Shapiro S., 2000, ApJ, 542, 453
Springel V., Hernquist L., 2003, MNRAS, 339, 312
Woods E., Loeb A., 1998, ApJ, 508, 760
Yokoyama J., 2003, astro-ph/0302263 v1
Yungelson L.R., Livio M., 2000, ApJ, 528, 108
Zwerger T., Müller E., 1997, A&A, 320, 209 (ZM)
Zwerger T., 1995, PhD thesis, Technische Universität München, Germany.